Impact of State-Specific Flowfield Modeling on Atomic Nitrogen Radiation

Christopher O. Johnston*
NASA Langley Research Center, Hampton, VA 23681

Marco Panesi†
University of Illinois at Urbana-Champaign, Urbana, IL 61801

(Dated: October 10, 2017)

A hypersonic flowfield model that treats electronic levels of the dominant afterbody radiator, N, as individual species is presented. This model allows electron-ion recombination rate and two-temperature modeling improvements, the latter which are shown to decrease afterbody radiative heating by up to 30%. This increase is primarily due to the addition of the electron-impact-excitation energy-exchange term to the energy equation governing the vibrational-electronic-electron temperature. This model also allows the validity of the often applied quasi-steady state (QSS) approximation to be assessed. The QSS approximation is shown to fail throughout most of the afterbody region for lower electronic states, although this impacts the radiative intensity reaching the surface by less than 15%. By computing the electronic state populations of N within the flowfield solver, instead of through the QSS approximation in the radiation solver, the coupling of nonlocal radiative transition rates to the species continuity equations becomes feasible. Implementation of this higher-fidelity level of coupling between the flowfield and radiation solvers is shown to increase the afterbody radiation by up to 50% relative to the conventional model.

I. INTRODUCTION

Considering Earth entry at velocities greater than 9 km/s, a recent study [1] showed the potential for significant radiative heating along the backshell or afterbody surface, with values of similar magnitude to the convective heating. Although this afterbody radiative heating component was deemed negligible (due to inadequate nonequilibrium radiation models) in previous NASA designs, it was indirectly accounted for with large convective heating margins [2, 3]. However, as afterbody heatshield design becomes more aggressive, with reduced convective heating margins, the importance of accurately modeling the afterbody radiation increases.

For Earth entry velocities above 9 km/s, afterbody radiation is dominated by atomic nitrogen (N) lines. Because of their strong sensitivity to the non-Boltzmann electronic state populations, the emission of N lines in a nonequilibrium expanding flow is challenging to accurately simulate. The present work addresses this challenge through the development of a flowfield model that treats electronic states of N as individual species in the flowfield. This state-specific flowfield model is in contrast to conventional flowfield models, where the total number density of N is computed by the flowfield solver, followed by the quasi-steady state [4] (QSS) computation of the electronic state number densities as a post-precessing step during the radiation computation. The state-specific model allows for the higher-fidelity treatment of three modeling sensitivities that impact the simulation of the non-Boltzmann electronic state populations and resulting radiation. These sensitivities are discussed in the following three paragraphs.

The first of these sensitivities is the rate of recombination of N^+ and e^- to form N. The faster the rate of recombination, the lower the radiation (because the population of upper emitting levels of N are proportional to N^+ and e^-). In the conventional flowfield model, this recombination rate is a function of temperature only. However, this rate is actually dependent on the upper electronic state number densities of N, which are dependent on both the electron number density and electron temperature [5, 6]. This is shown in Fig. 1, which compares the recombination rate for N, computed from the present non-Boltzmann model [7], for a range of electron number densities. For electron number densities below 1×10^{14} cm^{-3}, which exist for most afterbody conditions of interest, the recombination rate is seen to be a strong function of electron number density, as well as temperature. The state-specific model captures this behavior by treating flowfield ionization rates from individual (or grouped) levels of N.

The second of these sensitivities is the model for radiative transition rates between electronic states. These rates depend on both the local emission and the absorption of the incoming radiative intensity [8]. The complexity of treating this nonlocal absorption term has led to it typically being treated with approximate escape factors [4]. The state-specific model allows the nonlocal absorption term to be evaluated with a minimal increase in computational cost. This is a result of removing the computation of electronic-state populations from the radiation solver, therefore avoiding an iterative computation for this nonlocal absorption term. The state-specific model instead passes this term from the radiation solver

* christopher.o.johnston@nasa.gov; Aerospace Engineer
† Assistant Professor

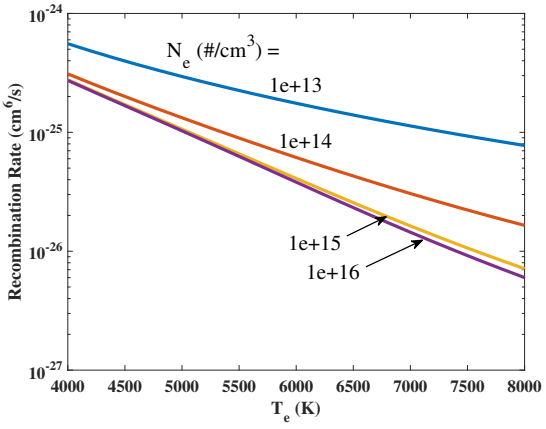

FIG. 1. Recombination rate for N at various electron number densities.

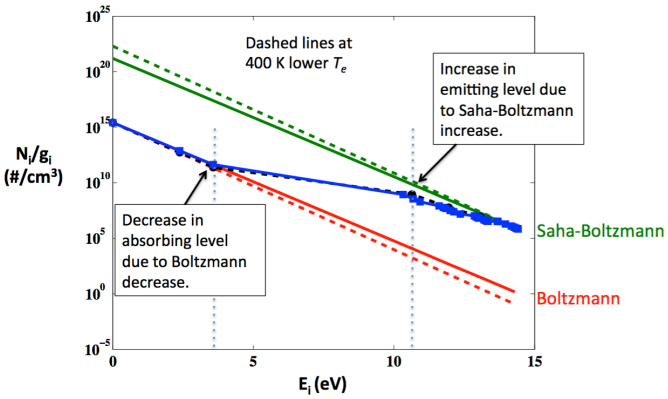

FIG. 2. Impact of a 400 K decrease in T_e on the population distribution of N at a representative afterbody condition.

to the flowfield solver every approximately 5000 flowfield iterations. This represents an additional level of radiation coupling, where for the conventional approach, only the divergence of the radiative flux is passed to the flowfield solver [9].

The third of these sensitivities is the free-electron temperature (T_e), which is used to evaluate the electron-impact transition and ionization rates. The sensitivity of the non-Boltzmann electronic state populations, and therefore the afterbody radiation, to T_e is significant. Figure 2 shows this sensitivity for a 400 K decrease in T_e, which results in an increase in the electronic state populations near 11 eV (seen by the slight increase in the black circle above the blue symbols). This increase is a result of the Saha-Boltzmann distribution increasing with decreasing temperature (assuming fixed number densities), which will be discussed in more detail later. The conventional flowfield model assumes that the free-electron, bound electronic, and vibrational temperatures are all equal to a single temperature, which is defined as T_{ve}. This temperature is computed from an energy equation that groups these energies. The state-specific model removes the bound electronic energy of N from this group, because the bound electronic energy of N is no longer defined by T_{ve}. Removing this energy requires the addition of an energy exchange term to account for electron-impact excitation processes. The addition of this new term makes T_{ve} more like T_e in strongly radiating afterbody regions, where molecular species (and therefore, vibrational energies) are negligible.

Details of the state-specific model are presented in Section II, which discusses both the collisional and radiative transition rates. The impact of the state-specific approach on the two-temperature model is presented in Section III. Finally, Section IV applies the state-specific model to a Stardust case [3, 10] and compares the results with the conventional flowfield model. The improved two-temperature modeling and treatment of nonlocal absorption are shown to have a notable impact on the afterbody radiation.

Note that the afterbody radiation is also sensitive to the rate model applied for the electron-impact transitions between electronic states. This model is composed of electron-impact excitation and ionization rates. Recent studies by Lopez et al. [11] have addressed these rates, so they will not be the subject of the present work (trends observed in the present work will apply to any rate model).

II. STATE-SPECIFIC FLOWFIELD MODEL FOR N

This section presents the state-specific flowfield model developed for N. To allow electronic states of N to be treated as individual species in the flowfield solver, the detailed 35 level model developed by Johnston et al. [7] is reduced to a more manageable 7 level model using the approach developed by Panesi and Lani [12]. The grouping applied to the present model is defined in Table I, where the grouped energy is defined as:

$$E_{i'} = \frac{\sum_{i \in G_{i'}} g_i E_i}{g_k} \tag{1}$$

The convention of this paper is that grouped levels are identified with a prime, such as i', while individual levels are not. The individual levels within a group are assumed to follow a Boltzmann distribution [12], which results in the following relationship between the group and individual number density:

$$N_i = N_{i'} \frac{g_i}{Q_{i'}} exp\left[-\frac{hc}{kT_e}(E_i - E_{i'})\right] \tag{2}$$

where

$$Q_{i'} = \sum_{i \in G_{i'}} g_i exp\left[-\frac{hc}{kT_e}(E_i - E_{i'})\right] \tag{3}$$

To model the 7 grouped number densities, $N_{i'}$, as individual species within the flowfield solver, rate models

for collisional and radiative processes are required. Development of these models are discussed in the following two subsections, while the third subsection discusses the implementation of these models in the LAURA/HARA code. Note that this implementation also requires modifications to the two-temperature model. These modifications are discussed in Section III.

A. Collisional Processes

Following Panesi and Lani [12], the electron-impact excitation rate between a lower grouped level i' and upper grouped level j', is written in terms of the rates between ungrouped levels i and j as follows:

$$k^{ex}_{i'j'} = \sum_{j\in G_{j'}} \sum_{i\in G_{i'}} \frac{k^{ex}_{ij} g_i}{Q_{i'}} exp\left[-\frac{hc}{kT_e}(E_i - E_{i'})\right] \quad (4)$$

The backward rate for this process is written in terms of the forward rate and the equilibrium constant:

$$k^{ex}_{j'i'} = \frac{k^{ex}_{i'j'}}{K^{ex}_{c,i'j'}} \quad (5)$$

where the equilibrium constant is:

$$K^{ex}_{c,i'j'} = \frac{Q_{j'}}{Q_{i'}} exp\left[-\frac{hc}{kT_e}(E_{j'} - E_{i'})\right] \quad (6)$$

Using the rates from the 35 level model developed by Johnston et al. [7], the grouped rates were computed and curve fit to the following form:

$$k^{ex}_{i'j'} = AT_e^n e^{-E/T_e} \quad (7)$$

while the equilibrium constant was fit to the following:

$$K^{ex}_{c,i'j'} = e^{\left(G_1/z + G_2 + G_3 log(z) + G_4 z + G_5 z^2\right)} \quad (8)$$

where z=10,000/T_e. The coefficients for these curve-fits are listed in Table III of the Appendix.

For an electron-impact ionization process from a grouped level i', the grouped forward rate is computed as

$$k^{ion}_{i'} = \sum_{i\in G_{i'}} \frac{k^{ion}_{i} g_i}{Q_{i'}} exp\left[-\frac{hc}{kT_e}(E_{ionize} - E_{i'})\right] \quad (9)$$

TABLE I. Details of the grouped level model for N.

Grouped Level, i'	Individual Levels, $G_{i'}$	$E_{i'}$ (eV)	$g_{i'}$
1	1	0.0	4
2	2	2.384	10
3	3	3.576	6
4	4 - 6	10.64	30
5	7 - 13	11.95	64
6	14 - 27	13.08	162
7	28 - 35	14.29	6578

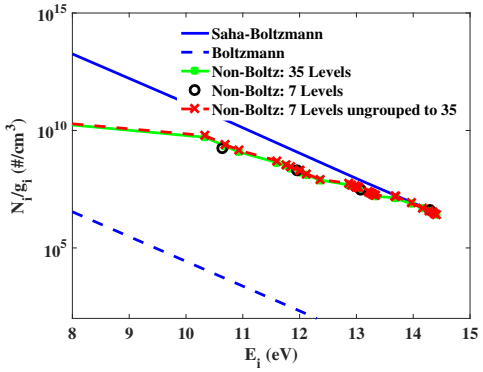

FIG. 3. Comparison of the population distribution of N resulting from 35 and 7 level models at a representative afterbody condition.

The recombination rate is computed using the equilibrium constant, which is written as:

$$K^{ion}_{c,i'} = \frac{2Q_+}{Q_{i'}} \left(\frac{2\pi mkT_e}{h^2}\right)^{3/2} exp\left[-\frac{hc(E_{ionize} - E_{i'})}{kT_e}\right] \quad (10)$$

The ionization rate and equilibrium constant are curve-fit to the form of Eqs. 7 and 8, respectively. The coefficients for these curve-fits are listed in Table IV.

In addition to these electron-impact excitation and electron-impact ionization processes, Tables V and VI in the Appendix present the rates applied for other processes. For the state-specific results presented in this paper, instances of N in Tables V and VI are replaced by the first grouped level of N, and the electron-impact ionization rate for N in Table VI (rate #8) is not applied.

To demonstrate the ability of the 7 level grouped model to reproduce the results of the full 35 level model, the QSS approach was applied to these two models for a condition representative of afterbody conditions. This condition consists of number densities for N, N^+, and e^- of 3.8×10^{15}, 1.5×10^{14}, 1.9×10^{14} particles/cm^3, respectively, and a T_{ve} of 4778 K. Figure 3 compares the results of the full 35 level model and the grouped 7 level model. Using Eq. 2, the 7 level results are ungrouped to 35 levels. Note that these ungrouped values are applied for the radiation computations. This figure shows that the ungrouped values are nearly identical to the 35 level model. This good agreement is the result of the 35 level model demonstrating Boltzmann distributions between grouped levels, which is implied in Eq. 2 for the 7 level model. The slight differences seen between the 35 level and ungrouped values impact the resulting radiation by less than 10% for the cases considered in this work, which is considered sufficient.

B. Radiative Processes

For each bound-bound radiative (atomic line) transition between upper level j and lower level i, the transi-

tion rate from j to i, resulting from spontaneous emission from j, is written as:

$$k_{ji}^{em} = A_{ji} \tag{11}$$

where A_{ji} is the Einstein coefficient for the transition, which is independent of temperature and number density. Transitions in the opposite direction, between lower level i and upper level j, are dependent on absorption of the radiative intensity resulting from the entire flowfield (I_ν) and the local line-shape (b_ν):

$$k_{ij}^{ab} = \int_0^\infty \frac{g_j b_\nu A_{ji} c^2 \int_{4\pi} I_\nu d\Psi}{8\pi h \nu^3} d\nu \tag{12}$$

The evaluation of this equation for a variable property tangent-slab is presented by Johnston [13], while Johnston and Mazaheri [14] discuss the application of a rigorous ray-tracing approach. Both the tangent-slab and ray-tracing approaches are computationally expensive because this term must be evaluated for every atomic line at every frequency and spatial point. Furthermore, treating this term requires numerous iterations due to its dependence on the rest of the flowfield.

Because of the difficulty in evaluating Eq. 12, this term is commonly approximated using the escape factor approach [15]. This approach assumes a constant property sphere around the point of interest, and no interaction between overlapping atomic lines. With these assumptions, Eq. 12 reduces to the following

$$k_{ij}^{ab} = A_{ji} \frac{N_j}{N_i} (1 - EF_{ij}) \tag{13}$$

where the escape factor, EF_{ij}, is defined as

$$EF_{ij} = \int_0^\infty \frac{exp(-\kappa_{\nu,ij} \Delta z)}{b_\nu} d\nu \tag{14}$$

For optically thin lines, EF_{ij} is equal to 1.0, while for optically-thick lines, such as those in the VUV, EF_{ij} is close to 0.0. Note that Eq. 14 does not allow for negative EF_{ij} values. This prevents the repopulation of upper levels, due to strong absorption of nonlocal emission, from being modeled. The impact of this repopulation will be discussed in Section IV.

Even though Eq. 12 does not explicitly use EF_{ij} values, they may be computed as a post-processing step as follows:

$$EF_{ij} = 1 - \frac{k_{ij}^{ab}}{k_{ji}^{em}} \frac{N_i}{N_j} \tag{15}$$

Comparing EF_{ij} values from the approximate and detailed approaches will provide insight into the impact of the nonlocal absorption term in Eq. 12, which represents the fundamental difference between the two approaches.

The above equations for radiative processes are written for the non-grouped electronic levels i and j. To convert these terms to transitions between grouped levels i' and j', as required for the state-specific flowfield model, the following equations are applied:

$$k_{j'i'}^{em} = \sum_{i \in G_{i'}} \sum_{j \in G_{j'}} \frac{k_{ji}^{em} g_j}{Q_{j'}} exp\left[-\frac{hc}{kT_e} (E_j - E_{j'}) \right] \tag{16}$$

$$k_{i'j'}^{ab} = \sum_{j \in G_{j'}} \sum_{i \in G_{i'}} \frac{k_{ij}^{ab} g_i}{Q_{i'}} exp\left[-\frac{hc}{kT_e} (E_i - E_{i'}) \right] \tag{17}$$

Applying these equations to a flowfield condition representative of a lunar-return flowfield, Table II lists values for $k_{j'i'}^{em} EF_{i'j'}$ and $EF_{i'j'}$ for each grouped level transition. This table shows the wide variation in the magnitude of $EF_{i'j'}$ for the various transitions. With the exception of the 6-5 transition, the largest $k_{j'i'}^{em} EF_{i'j'}$ values are seen for transitions with i'=3 and j' larger than 3, which represent vacuum ultraviolet (VUV) transitions. Unlike transitions with i' equal to 1 or 2, which are deeper into the VUV, the $EF_{i'j'}$ values for i'=3 transitions are greater than 0.2. These relatively large $EF_{i'j'}$ values for VUV transitions, particularly the 4-3 transition, will be shown later in this paper to have a significant impact on the radiative environment.

C. Implementation of the State-Specific Model for N in LAURA/HARA

The implementation of the collisional transition rates, discussed in subsection A, within the LAURA/HARA code [16] is relatively straightforward. The species source term due to these collisions is written as:

$$\left(\frac{\partial N_{i'}}{\partial t} \right)_{col} = \sum_{j'=1}^{m} k_{j'i'}^{ex} N_{j'} N_e - \sum_{j'=1}^{m} k_{i'j'}^{ex} N_{i'} N_e - \sum_{j'=1}^{m} k_{i'}^{ion} N_{i'} N_e + \sum_{j'=1}^{m} \frac{k_{i'}^{ion}}{K_{c,i'}^{ion}} N_+ N_e^2 \tag{18}$$

The rates in this equation are implemented analogously to conventional flowfield rates, with the 7 grouped levels of N identified within the code as "N_i", where 'i' is

TABLE II. Radiative transition rates for the grouped N model at an afterbody flowfield condition ($k_{j'i'}^{em} EF_{i'j'}$ has units of mole^{-1}s^{-1}).

j'	i'	$k_{j'i'}^{em} EF_{i'j'}$	$EF_{i'j'}$	j'	i'	$k_{j'i'}^{em} EF_{i'j'}$	$EF_{i'j'}$
4	1	7.6e+0	2.6e-8	6	4	6.3e+4	7.1e-1
4	2	1.8e+5	3.3e-3	6	5	9.5e+6	4.1e-1
4	3	6.6e+6	3.2e-1	7	1	9.6e+1	8.6e-5
5	2	7.9e+4	4.2e-3	7	2	5.5e+4	7.6e-2
5	3	1.2e+6	4.4e-1	7	3	6.6e+5	1.0e+0
5	4	4.2e+5	1.7e-2	7	4	3.1e+4	7.6e-1
6	1	7.9e+2	3.1e-5	7	5	8.3e+5	1.0e+0
6	2	7.0e+5	2.7e-2	7	6	3.8e+5	1.0e+0
6	3	6.4e+6	6.5e-1				

the group number. The presence of the underscore differentiates the grouped level from conventional species. Note that transport properties for the grouped levels are assumed equal to N.

In contrast to the collisional transition rates, implementation of the radiative transition rates requires an advanced level of coupling between the LAURA flowfield code and HARA radiation code. Within the LAURA code, the following radiative source term is added to the species continuity equations:

$$\left(\frac{\partial N_{i'}}{\partial t}\right)_{rad} = \sum_{j'=i'+1}^{m} (k^{em}_{j'i'} N_{j'} - k^{ab}_{i'j'} N_{i'}) + \sum_{j'=1}^{i'-1} (k^{ab}_{j'i'} N_{j'} - k^{em}_{i'j'} N_{i'}) \quad (19)$$

The transition rates due to emission ($k^{em}_{i'j'}$) and absorption ($k^{ab}_{j'i'}$) are computed in HARA using Eqs. 11-17. These rates are then sent to LAURA for implementation in Eq. 19. After a defined number of LAURA flowfield iterations, typically around 5000, the rates are recomputed in HARA. This process is repeated until convergence. This represents an additional level of coupling between LAURA and HARA, as typically only the divergence of the radiative flux is passed from HARA to LAURA. Furthermore, the following two options for computing $k^{ab}_{j'i'}$ have been implemented:

1. *approximate EF*: Computes $k^{ab}_{j'i'}$ using escape factors from Eq. 14.
2. *detailed EF*: Computes $k^{ab}_{j'i'}$ using Eq. 12. The tangent-slab approximation is applied to evaluate this term.

Note that, by removing the quasi-steady state computation for the population of the N levels in HARA, the state-specific approach makes feasible the detailed treatment of radiative transition rates using either the tangent-slab approximation or the ray-tracing approach.

III. REQUIRED MODIFICATIONS TO THE TWO-TEMPERATURE MODEL

By modeling electronic states of N as individual species in the flowfield, therefore making their electronic energy independent of the flowfield vibrational-electronic temperature, T_{ve}, modifications are required to the definition of T_{ve} and its governing energy equation. The temperature T_{ve} is defined for the state-specific N flowfield assuming equilibration between the vibrational energy modes of all molecules, the free electron translational energy, and the bound electronic energy of atoms and molecules other than N. In other words, T_{ve} is defined identically to the approach presented by Gnoffo et al. [17], except the bound electronic states of N are no longer governed by this temperature because they are treated as individual species in the species continuity equation, which determines the population of each electronic level. Note that these bound electronic states of N are included in the total energy equation.

The conservation equation for the energy governed by T_{ve} is written similarly to the conventional vibrational-electronic energy equation defined by Gnoffo et al. [17] The "vibrational-electronic" source terms are written as

$$\text{Source Terms} = R_{V-T} + R_{e-T} + S_V + \Omega_I + \Omega_E + Q_{rad} \quad (20)$$

where the R_{V-T}, R_{e-T}, and S_V terms are the vibrational-translational energy relaxation, electron-translational energy relaxation, and vibrational energy reactive source terms, respectively, and do not require modification. The modification of the other three terms are discussed below.

A. Electronic Energy Reactive Source Term

The Ω_I term is the electronic energy reactive source term, which is written by Gnoffo et al. [17] as

$$\Omega_I = -\sum_{s=ions} \dot{n}_{e,s} I_s \quad (21)$$

where $\dot{n}_{e,s}$ is the production rate of ion s from the respective electron-impact ionization reaction and I_s is the ionization energy between the associated neutral atom and the ion s. This term is present in the conventional two-temperature model because the heats of formation of ions (and all species) are not included in the vibrational-electronic enthalpy, even though the heats of formation of ions include electronic energy equal to I_s. This term therefore accounts for this electronic energy implied by the heat of formation and allows for I_s to be chosen as a value lower than that assuming ionization from the ground state. For the present modified approach, the form of this term is the same, but the meaning is different for N. Electron-impact ionization processes result in a transfer of energy between free-electrons and bound electronic states, which are in different energy pools for N (unlike the conventional case) and therefore require this energy exchange term. The value of I_s for each electronic state of N is applied, therefore avoiding the need to assume a value, as required in the conventional approach.

B. Electron-Impact Excitation Energy Exchange

The Ω_E term is the electron-impact excitation energy exchange term, which accounts for energy exchange when the impact of free-electrons causes a change between two bound electronic levels of N. This term is written as

$$\Omega_E = -\sum_{i'=1}^{N_E-1} \sum_{j'=i+1}^{N_E} \dot{n}_{e,i',j'} (E_{j'} - E_{i'}) \quad (22)$$

where $\dot{n}_{e,i',j'}$ is the electron-impact transition rate between lower level i' and upper level j'. Note that this term is not required in the conventional approach described by Gnoffo et al. [17] because bound electronic levels of N and free-electron translational energy are both governed by T_{ve}.

C. Divergence of the Radiative Flux

The radiative source term for the total energy equation is the divergence of the radiative flux, which is written as:

$$Q_{rad} = 4\pi j_\nu - \kappa_\nu \int_{4\pi} I_\nu d\Psi \tag{23}$$

For the conventional two-temperature model, this term is also applied to the vibrational-electronic energy equation, as a result of all significant radiative transitions being between vibrational or electronic states. For the present state-specific N model, however, an altered radiative source term (Q^{VE}_{rad}), which removes energy from bound-bound radiative transitions of N, is required for the vibrational-electronic energy equation. This term may be computed based on the radiative transition rates for N in Eqs. 11 - 17 as follows:

$$Q^{VE}_{rad} = Q_{rad} - \sum_{i'=1}^{m} \sum_{j'=i'+1}^{m} (k^{em}_{j'i'} N_{j'} - k^{ab}_{i'j'} N_{i'}) hc(E_{j'} - E_{i'}) \tag{24}$$

This representation is convenient because it avoids evaluating additional computationally expensive terms. The summation term, which represents the energy from bound-bound radiative transitions of N, will be referred to as $Q_{rad,N}$ in the following sections.

IV. IMPACT OF THE STATE-SPECIFIC MODEL ON STARDUST AT 46 S

This section examines the differences in the radiative environment, predicted by the conventional and state-specific approaches, for the Stardust capsule at the 46 s trajectory point (11.69 km/s, 1.05×10^{-4} kg/m^3). This case was considered in previous studies by Johnston and Brandis [1] and West et al. [18]. Figure 4 defines the three lines-of-sight that will be studied throughout this section. In subsection A, the impact of the QSS approximation will be studied for the stagnation-line and afterbody lines-of-sight. This is followed in subsection B by the study of energy equation modifications required by the state-specific approach, as presented in the previous section. Finally, subsection C examines the impact of treating nonlocal (or detailed) escape factors instead of the commonly applied local approximation.

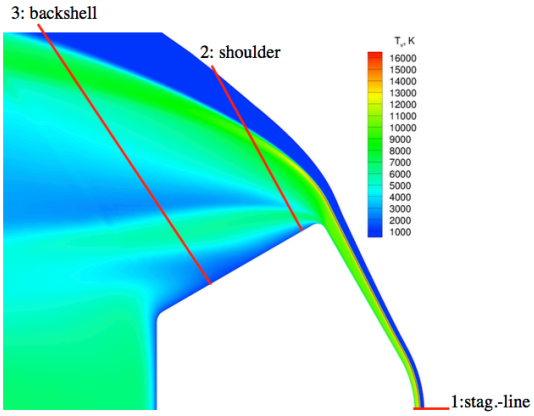

FIG. 4. Line-of-sight definitions for the Stardust case.

A. Influence of Removing the QSS Assumption

This subsection examines the validity of the QSS approximation [4], which is used by the conventional approach to compute the population distribution of N. The state-specific approach developed in this work avoids this approximation, and therefore provides a benchmark for comparison.

The QSS approximation assumes that the inflow and outflow rates from each level, due to collisional and radiative processes, are significantly larger than the total rate of change of each level. The inflow and outflow rates are defined from Eqs. 18 and 19 as follows:

$$S_{inflow,i'} = \sum_{j'=1}^{m} k^{ex}_{j'i'} N_{j'} N_e + \sum_{j'=1}^{m} \frac{k^{ion}_{i'}}{K^{ion}_{c,i'}} N_+ N_e^2 + \sum_{j'=i'+1}^{m} k^{em}_{j'i'} N_{j'} + \sum_{j'=1}^{i'-1} k^{ab}_{j'i'} N_{j'} \tag{25}$$

$$S_{outflow,i'} = \sum_{j'=1}^{m} k^{ex}_{i'j'} N_{i'} N_e + \sum_{j'=1}^{m} k^{ion}_{i'} N_{i'} N_e + \sum_{j'=i'+1}^{m} k^{ab}_{i'j'} N_{i'} + \sum_{j'=1}^{i'-1} k^{em}_{i'j'} N_{i'} \tag{26}$$

while the total rate of change of each level is defined as

$$\frac{\partial N_{i'}}{\partial t} \equiv \frac{\partial N_{i'}}{\partial x} u + \frac{\partial N_{i'}}{\partial y} v + \frac{\partial N_{i'}}{\partial z} w \tag{27}$$

Therefore, the QSS approximation is valid when the following inequalities are satisfied:

$$S_{inflow,i'} >> \frac{\partial N_{i'}}{\partial t} \tag{28}$$

$$S_{outflow,i'} >> \frac{\partial N_{i'}}{\partial t} \tag{29}$$

For the stagnation-line and afterbody lines-of-sight, defined in Fig. 4, Figs. 5(a) and 6(a) compare $S_{inflow,i'}$ and $\frac{\partial N_{i'}}{\partial t}$ for the first 3 levels of N (comparisons with $S_{outflow,i'}$, instead of $S_{inflow,i'}$, provide identical conclusions). These values are computed using the state-specific flowfield. For a given level i', the QSS approximation is valid for regions where the dashed line is larger than the solid line. This inequality is seen to hold for the stagnation-line between 0.2 and 1.0 cm. The afterbody line-of-sight, however, does not satisfy this inequality, because the lower temperatures decrease the collisional rates (and therefore $S_{inflow,i'}$) considerably. Figures 5(b) and 6(b) make the same comparison for the 4th and 5th levels of N, which are strong emitters. These figures show that the QSS approximation holds for these upper levels in regions of both the stagnation-line and afterbody lines-of-sight.

Figures 5(c) and 6(c) compare the level number densities for N resulting from the state-specific and QSS approaches. To make a meaningful comparison, the same state-specific flowfield is applied for both the state-specific and QSS approaches. By summing the number densities of all N levels resulting from the state-specific flowfield, the QSS approximation is applied to the non-Boltzmann level computation in a manner consistent with the conventional approach. These figures show that QSS breakdown near the wall and shock result in noticeable errors in the resulting level number densities (for the afterbody case, these errors are noticeable across the entire layer). The impact of these differences in the wall-directed intensity is examined in Figs. 5(d) and 6(d). For the stagnation-line, Fig. 5(d) shows that the impact of the QSS approximation on the intensity is negligible. The regions near the shock and wall that showed a QSS breakdown do not contain significant emission or absorption from N, because of the low number densities of N in these regions. For the afterbody line of sight, Fig. 6(d) shows that the QSS approximation results in noticeable errors throughout the layer, although the impact on the radiative intensity reaching the wall is less than 15%. This relatively small impact is again the result of the low number densities in regions with large QSS errors.

B. Influence of Energy Equation Modifications

For each of the lines-of-sight defined in Fig. 4, the temperatures, Φ, and wall-directed radiative intensity resulting from the conventional and state-specific approaches are compared in Figs. 7–10. These figures also present the vibrational-electronic source terms, from Eq. 20, for the state-specific model. Note that Φ was defined by

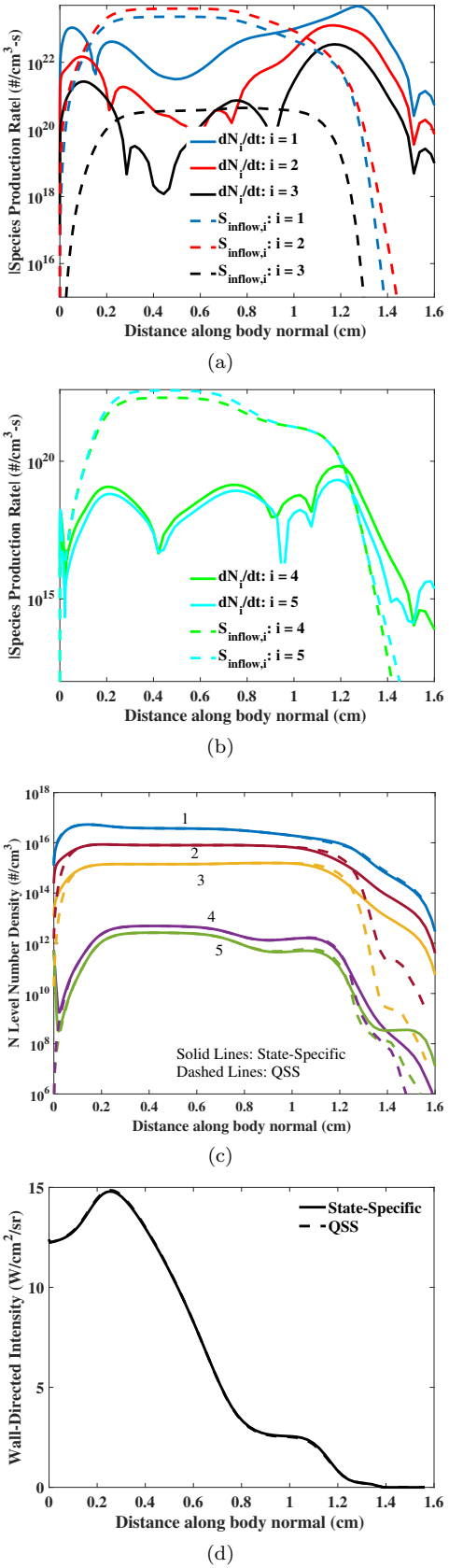

FIG. 5. Impact of the QSS approximation on the stagnation-line.

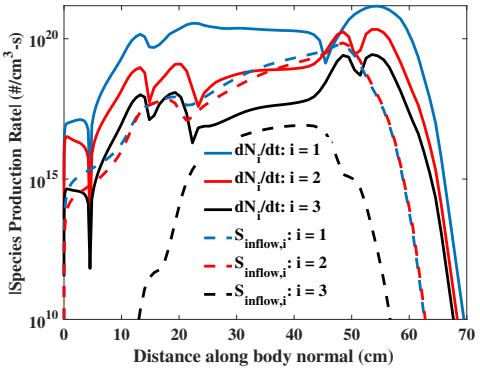

(a)

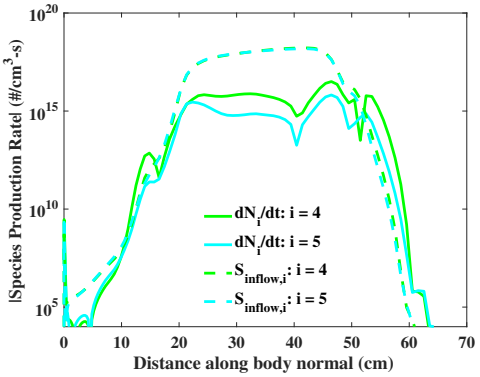

(b)

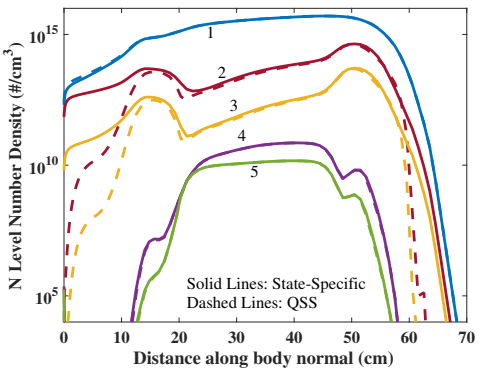

(c)

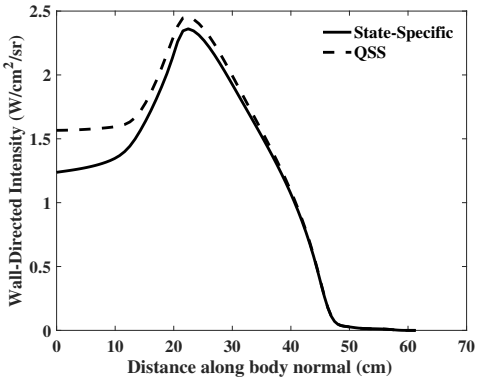

(d)

FIG. 6. Impact of the QSS approximation on the afterbody line-of-sight.

Johnston and Brandis [1] as

$$\Phi = log_{10}\left(\frac{N_j^{SB}}{N_j^{B}}\right) = log_{10}\left[\frac{N_{N+}N_e}{N_N}\frac{Q_a}{2Q_+}\left(\frac{h^2}{2\pi mkT_{ve}}\right)^{3/2} exp\left(\frac{hc}{kT_{ve}}E_{ionize}\right)\right] \quad (30)$$

This value represents the order-of-magnitude difference between the Boltzmann and Saha-Boltzmann distributions for N. As discussed by Johnston and Brandis [1], larger positive values of Φ result in stronger N emission.

Figure 7 compares these properties along the stagnation-line. The larger separation between T_{tr} and T_{ve} for the state-specific approach indicates a larger region of post-shock thermochemical nonequilibrium. This increased nonequilibrium region is the result of adding Ω_E, which accounts for the loss of free-electron energy when free electron collisions excite N. Recall that this term is not present in the conventional model because the free-electron energy is grouped with the bound electronic energy of N. In the post-shock region between 0.8 and 1.4 cm, electronic states of N are being excited by electron collisions, therefore resulting in the negative Ω_E values seen in Fig. 7(b). To counteract these negative Ω_E values, the R_{e-T} and R_{V-T} source terms are increased through increased positive values of $T_{tr} - T_{ve}$ (R_{e-T} and R_{V-T} are proportional to this difference). This increased difference between T_{tr} and T_{ve}, resulting from the introduction of Ω_E, is one of most significant differences between the state-specific and conventional models.

Through the exponential term in Eq. 30, Φ increases with decreasing T_{ve}, assuming fixed number densities. This implies the counterintuitive trend that the radiative emission increases with decreasing T_{ve}, which holds for non-Boltzmann atomic species (this was mentioned in the discussion of Fig. 2 in the Introduction). Figures 7(a) and (c) demonstrate the smaller (more negative) Φ values resulting from the larger T_{ve} values for the state-specific approach (the large positive Φ values between 1.3 and 1.5 cm may be ignored, since the electron number densities and resulting emission are negligible in this early post-shock region). The negative Φ values between 0.8 and 1.2 cm are characteristic of a compressing nonequilibrium post-shock region. The more negative Φ values for the state-specific approach between 0.7 and 0.9 cm result in less emission. The lower emission in this region for the state-specific approach is shown in Fig. 7(d) to result in lower wall-directed intensity reaching the surface. Note that this lower radiative intensity, which corresponds to a lower radiative heating, is primarily a result of adding Ω_E for the state-specific approach.

The same set of figures as presented in Fig. 7 for the stagnation line are presented in Figs. 9 and 10 for the shoulder and afterbody lines-of-sight, respectively. Unlike the stagnation-line, the shoulder and afterbody lines-of-sight are entirely in thermochemical nonequilibrium,

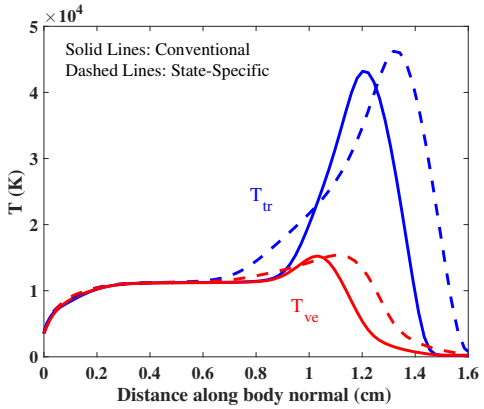

(a)

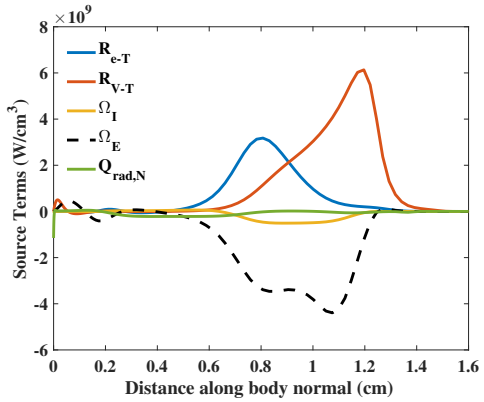

(b)

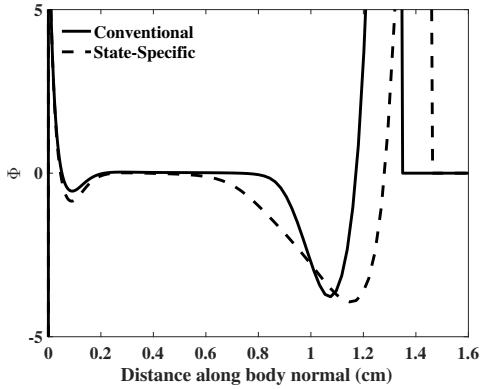

(c)

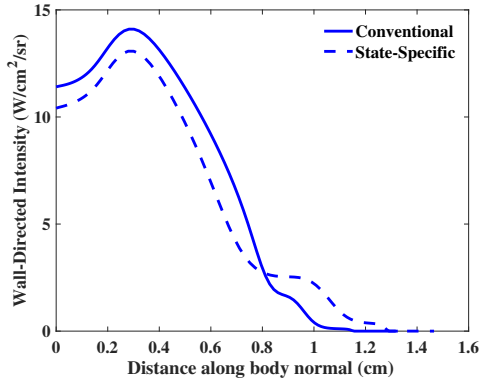

(d)

FIG. 7. Profiles along the stagnation-line for the Stardust case.

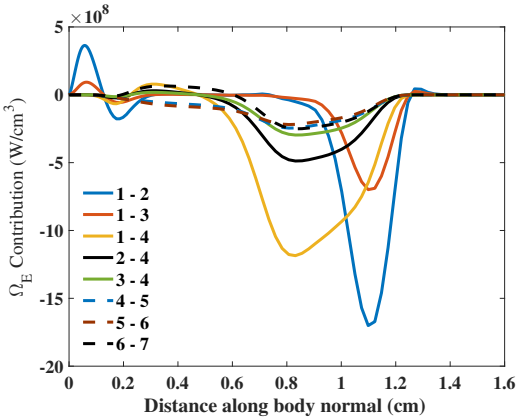

FIG. 8. Contributions to Ω_E from each electron-impact excitation process of N for the stagnation line.

as indicated by T_{tr} and T_{ve} remaining separate, as well as the nonzero values of Φ. For the shoulder or afterbody lines-of-sight the strongest radiative emission occurs in regions of expanding nonequilibrium flow, characterized by positive values of Φ and negative values of $T_{tr} - T_{ve}$. This is in contrast to the stagnation-line (and most of the forebody), where the strongest emission occurs in equilibrium or compressing nonequilibrium regions. In this expanding nonequilibrium flow, the electron-impact processes are de-populating the upper levels of N, therefore resulting in positive values of Ω_E. Similarly to the stagnation region, where negative Ω_E values are counteracted by increased positive values of $T_{tr} - T_{ve}$, the positive Ω_E values are counteracted by increased negative values of $T_{tr} - T_{ve}$. This results in the negative R_{e-T} values seen in Figs. 9(b) and 10(b), that are of similar magnitude to Ω_E.

For the afterbody line-of-sight, the region between 10 and 25 cm follows a trend opposite to that discussed in the previous paragraph. In this region, the state-specific model predicts a decreased difference between T_{tr} and T_{ve} (instead of the increased difference seen above 25 cm). This region consists of low electron and ion number densities, therefore preventing large values for Ω_E and R_{e-T}. Instead, this region is impacted most by strong radiative absorption, indicated by positive $Q_{rad,N}$ values. For the conventional approach, $Q_{rad,N}$ is included in the vibrational-electronic energy equation, therefore resulting in increased T_{ve} values in regions of strong absorption. For the state-specific approach, however, the bound-bound radiative energy transfer from N, represented by $Q_{rad,N}$, is removed from the vibrational-electronic energy equation. This results in the decreased T_{ve} for the state-specific approach seen in Fig. 10(a) between 10 and 25 cm.

The differences between the T_{ve} values predicted by the state-specific and conventional approaches discussed in the previous two paragraphs are seen in Figs. 9(c) and 10(c) to have the expected impact on the Φ comparison, where Φ increases with decreasing T_{ve}. With the local

radiative emission roughly proportional to Φ, the comparison between the state-specific and conventional wall-directed radiative intensites in Figs. 9(d) and 10(d) may be interpreted. Throughout the region where Ω_E dominates, which increases T_{ve} and therefore decreases Φ, the emission and resulting intensity is lower for the state-specific approach. For the shoulder line-of-sight, which is impacted negligibly by $Q_{rad,N}$, Fig. 9(d) shows that the radiative intensity reaching the surface is therefore lower for the state-specific approach. For the afterbody line-of-sight, the T_{ve} decrease in the separated region, due to $Q_{rad,N}$, results in larger Φ values for the state-specific approach. This region around 15 cm leads to less absorption for the state-specific approach, although the radiative intensity reaching the surface remains 30% lower because of the Ω_E dominated region.

An issue not yet addressed in this section is the impact of the state-specific approach on the (electron number density dependent) electron-impact ionization/recombination rate (shown in Fig. 1 and discussed in the Introduction). For the afterbody line-of-sight, Fig. 11 compares the electron number density resulting from the conventional and state-specific models. Considering the large differences in T_{ve} shown in Fig. 10(a) and the electron number density dependency, the agreement is relatively good. This agreement suggests that the recombination occurring at electron number densities below 1×10^{15} cm^{-3}, where Fig. 1 shows an electron number density dependency, is negligible.

Note that the results presented so far apply the approximate escape factor (EF) approach discussed in Section II B, which is applied identically in the conventional and state-specific approaches. The following subsection will investigate the differences resulting from the approximate and detailed EF approaches.

C. Influence of Detailed Escape Factors

As a result of the relatively low electron number densities present in the shoulder and afterbody regions of the flow, the radiative transition rates between electronic states discussed in Section II B have a significant impact on the upper level populations of N. Typical conventional radiation simulations apply the approximate escape factor (EF) approach, represented by Eqs. 13 and 14, which, for each atomic line, computes an EF value at each spatial point in the flow based on only properties at that point. The more rigorous or detailed approach, represented by Eqs. 12 and 15, computes the transition rates at each spatial point based on the incoming radiative intensity from the surrounding flow. This approach is too computationally expensive when applied to the conventional approach, as a result of the required iterative QSS computations, so it has not been typically applied nor has its impact been assessed, with the exception of the study by Sohn et al. [8] for DSMC flows. However, its impact is potentially significant because the nonlocal na-

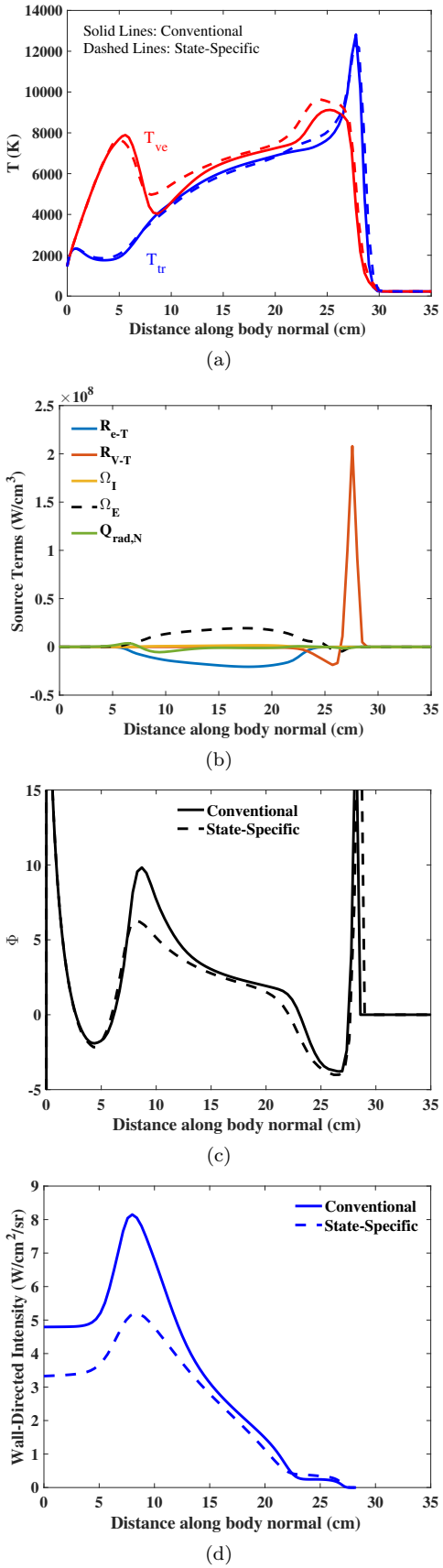

FIG. 9. Profiles along the shoulder for the Stardust case.

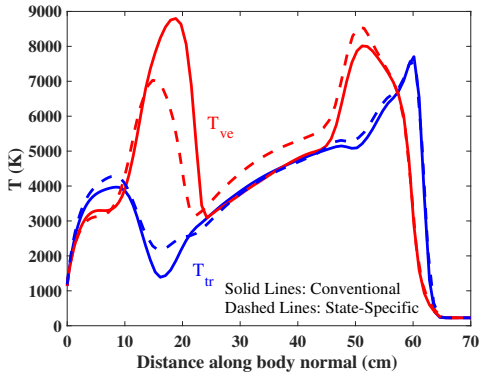

(a)

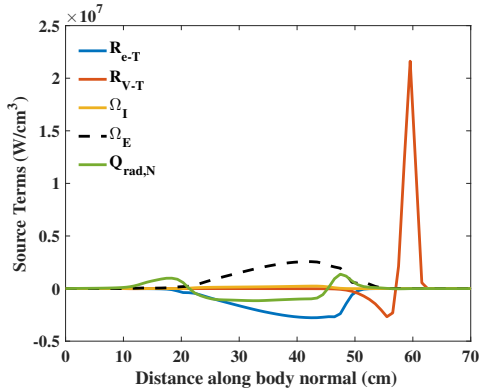

(b)

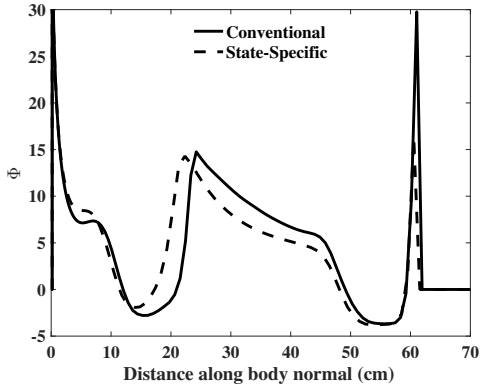

(c)

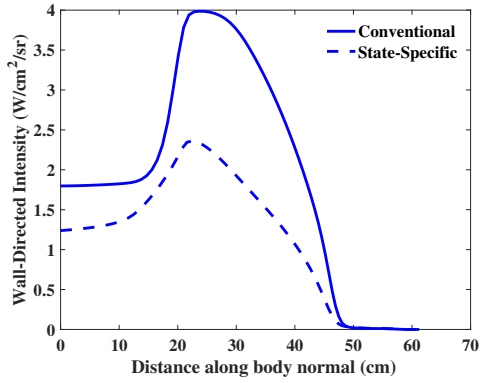

(d)

FIG. 10. Profiles along the afterbody for the Stardust case.

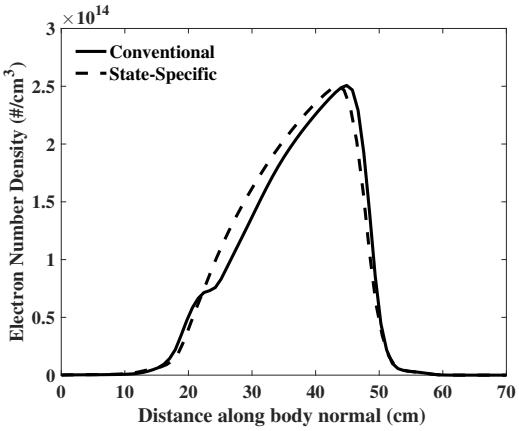

FIG. 11. Comparison in electron number density along the afterbody line-of-sight.

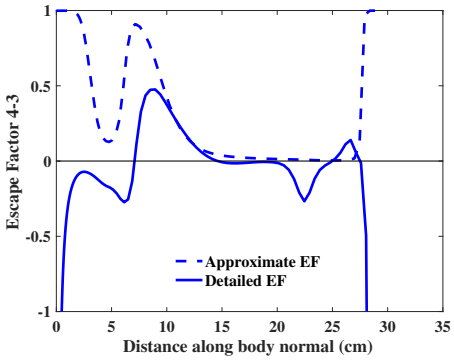

(a)

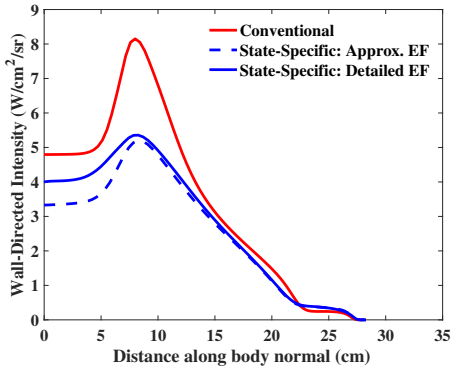

(b)

FIG. 12. Impact of detailed escape factor treatment for shoulder line-of-sight.

ture may capture the impact of radiation from strongly emitting regions being absorbed by nearby weakly emitting regions, and therefore causing an increase in the local emission.

To examine the difference between approximate and detailed EF approaches, Figs. 12(a) and 13(a) compare the EF values for the dominant 4-3 transition for the shoulder and afterbody lines-of-sight. The tangent-slab approximation is applied to evaluate Eq. 12 for the de-

tailed EF approach. Note that EF values for the approximate EF approach can only vary between 0.0 and 1.0. A value of 1.0 indicates an optically-thin location, which provides the maximum depopulation of the upper level 4, and 0.0 indicates an optically thick location, which nullifies the radiative transition between levels 3 and 4. For the detailed EF approach, however, there is no lower limit for EF (although the upper limit remains 1.0). Negative values indicate that the transition rate due to absorption, which represents transitions from levels 3 to 4, is larger than the transition rate due to emission, which represents transitions from levels 4 to 3. Figures 12(a) and 13(a) show that the EF values are closest near the strongly emitting center of the shock layer. In addition to being strongly radiating, these regions have weaker gradients in temperatures and number densities, which make them more consistent with the approximations made in the derivation of the approximate EF approach. Outside of this center region, however, the detailed approach predicts significant absorption, represented by negative EF values, which the approximate EF approach is unable to model.

The consequence of the negative escape factors predicted by the detailed model, which repopulate the strongly emitting level 4, is apparent in the wall-directed radiative intensity profiles presented in Figs. 12(b) and 13(b). These figures compare the state-specific intensity resulting from the approximate and detailed EF approaches (the result of the conventional approach, for which only the approximate result is available, is presented for reference). For the higher density shoulder line-of-sight, Fig. 12(b) shows only a 5% difference between the approximate and detailed EF approaches, which is primarily due to negative EF values around 5 cm. For the lower density afterbody line-of-sight, Fig. 13(b) shows a nearly 100% increase in the radiative intensity reaching the surface for the detailed EF approach, which is due to negative EF values near the shock and boundary layer.

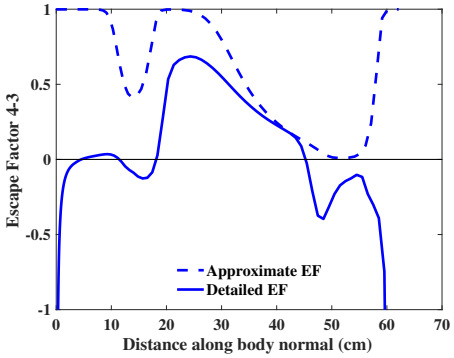

(a)

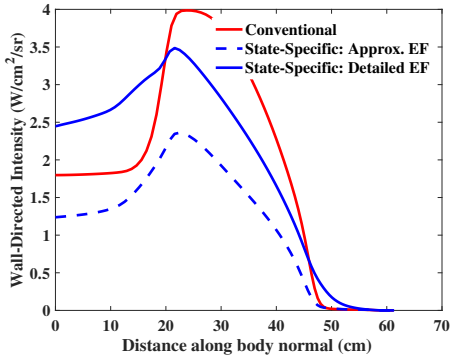

(b)

FIG. 13. Impact of detailed escape factor treatment for afterbody line-of-sight.

V. CONCLUSIONS

A flowfield model that treats electronic states of N as individual species was developed. This enables improvements in the two-temperature modeling, which result in a 10 - 30% decrease in the afterbody radiation. This model also allows the validity of the QSS approximation to be assessed. In afterbody regions, the QSS approximation is shown to fail because of the low temperatures, which decrease the electron-impact excitation rates. However, this failure is shown to impact the radiative intensity reaching the surface by less than 15%. The state-specific model makes possible, with a minimal increase in computational cost, the detailed treatment of radiative absorption on the non-Boltzmann model, representing detailed escape factors. For low density wake conditions, the detailed escape factor approach increases the radiation by over 50% relative to the conventional flowfield.

VI. ACKNOWLEDGMENTS

The present work was funded by the NASA Space Technology Mission Directorate Entry Systems and Modeling (ESM) project, with tasks leads Michael Wright and Michael Barnhardt. Comments on this work by Victor Lessard, Kelly Murphy, and Thomas West of NASA Langley are gratefully acknowledged.

APPENDIX

Appendix A: State-Specific Rates for N

Tables III and IV present the coefficients for Eqs. 7 and 8 developed for the electron-impact excitation and ionization rates, respectively. These rates represent the state-specific model developed in the present work for N. The forward rates have units of $\mathrm{cm}^3\mathrm{mole}^{-1}\mathrm{s}^{-1}$.

TABLE III. Electron-impact excitation rates for N.

i'	j'	A	n	E	G_1	G_2	G_3	G_4	G_5
1	2	1.406e+13	5.571e-01	2.76780e+04	1.77636e-15	9.16291e-01	-2.93099e-14	-2.76780e+00	-4.08007e-15
1	3	2.324e+15	-1.475e-02	4.15131e+04	2.84217e-14	4.05465e-01	-6.75016e-14	-4.15131e+00	-4.88498e-15
1	4	2.085e+21	-1.136e+00	1.23544e+05	-1.05989e-01	1.91969e+00	-2.78234e-01	-1.21187e+01	1.41200e-02
1	5	9.717e+15	-3.703e-02	1.38746e+05	-4.04740e-02	2.72563e+00	-1.12245e-01	-1.37679e+01	1.04969e-02
1	6	2.992e+14	3.272e-01	1.51840e+05	-1.57976e-02	3.68556e+00	-4.23075e-02	-1.51463e+01	7.81791e-03
1	7	3.160e+17	-4.979e-01	1.65937e+05	8.76378e-02	7.50474e+00	2.42279e-01	-1.68200e+01	6.07758e-02
2	3	9.684e+14	2.191e-01	1.38351e+04	4.08562e-14	-5.10826e-01	7.63833e-14	-1.38351e+00	3.60822e-15
2	4	3.487e+17	-3.784e-01	9.58655e+04	-1.05989e-01	1.00340e+00	-2.78234e-01	-9.35085e+00	1.41200e-02
2	5	3.378e+16	-1.152e-01	1.11068e+05	-4.04740e-02	1.80934e+00	-1.12245e-01	-1.10001e+01	1.04969e-02
2	6	3.520e+15	1.218e-01	1.24162e+05	-1.57976e-02	2.76926e+00	-4.23075e-02	-1.23785e+01	7.81791e-03
2	7	5.085e+17	-4.992e-01	1.38259e+05	8.76378e-02	6.58845e+00	2.42279e-01	-1.40522e+01	6.07758e-02
3	4	2.758e+17	-3.356e-01	8.20304e+04	-1.05989e-01	1.51423e+00	-2.78234e-01	-7.96734e+00	1.41200e-02
3	5	2.224e+16	-7.572e-02	9.72332e+04	-4.04740e-02	2.32016e+00	-1.12245e-01	-9.61659e+00	1.04969e-02
3	6	2.858e+15	1.650e-01	1.10327e+05	-1.57976e-02	3.28009e+00	-4.23075e-02	-1.09950e+01	7.81791e-03
3	7	6.708e+17	-5.000e-01	1.24424e+05	8.76378e-02	7.09927e+00	2.42279e-01	-1.26687e+01	6.07758e-02
4	5	6.243e+16	2.514e-01	1.52027e+04	6.55146e-02	8.05935e-01	1.65989e-01	-1.64925e+00	-3.62308e-03
4	6	7.237e+15	3.224e-01	2.82967e+04	9.01909e-02	1.76586e+00	2.35927e-01	-3.02764e+00	-6.30205e-03
4	7	2.662e+18	-3.454e-01	4.23932e+04	1.93626e-01	5.58505e+00	5.20513e-01	-4.70136e+00	4.66559e-02
5	6	2.811e+17	2.011e-01	1.30940e+04	2.46764e-02	9.59928e-01	6.99376e-02	-1.37839e+00	-2.67897e-03
5	7	2.497e+19	-4.488e-01	2.71905e+04	1.28112e-01	4.77911e+00	3.54524e-01	-3.05211e+00	5.02790e-02
6	7	8.076e+20	-5.740e-01	1.40965e+04	1.03435e-01	3.81918e+00	2.84586e-01	-1.67372e+00	5.29579e-02

TABLE IV. Electron-impact ionization rates for N.

i'	A	n	E	G_1	G_2	G_3	G_4	G_5
1	1.241e+13	4.326e-01	1.68905e+05	1.23478e-01	-4.15111e+00	-1.57524e+00	-1.68239e+01	-6.60695e-03
2	1.334e+13	3.850e-01	1.41227e+05	1.23478e-01	-5.06740e+00	-1.57524e+00	-1.40561e+01	-6.60695e-03
3	2.061e+13	3.578e-01	1.27392e+05	1.23478e-01	-4.55658e+00	-1.57524e+00	-1.26726e+01	-6.60695e-03
4	3.019e+13	8.985e-01	4.53614e+04	2.29467e-01	-6.07080e+00	-1.29701e+00	-4.70525e+00	-2.07269e-02
5	1.487e+14	8.267e-01	3.01587e+04	1.63952e-01	-6.87674e+00	-1.46300e+00	-3.05600e+00	-1.71038e-02
6	1.260e+15	7.322e-01	1.70647e+04	1.39276e-01	-7.83667e+00	-1.53293e+00	-1.67761e+00	-1.44249e-02
7	5.018e+18	2.437e-01	2.96823e+03	3.58407e-02	-1.16559e+01	-1.81752e+00	-3.89284e-03	-6.73828e-02

Appendix B: Flowfield Chemistry

Tables V and VI present the flowfield chemistry applied in this work for the conventional flowfield cases. For the state-specific cases, the same rates are applied, except for the electron-impact ionization rate for N. Furthermore, the reactions involving N are replaced by the ground state of N, or level 1. The forward rates have units of $\mathrm{cm^3 mole^{-1} s^{-1}}$.

[1] C. O. Johnston and A. M. Brandis, Journal of Spacecraft & Rockets **52**, 105 (2015).

[2] R. B. Erb, D. H. Greenshields, and L. T. Chauvin, *Apollo Thermal Protection System Development*, AIAA Paper 1968–1142 (1968).

[3] D. Olynick, Y.-K. Chen, and M. E. Tauber, Journal of Spacecraft & Rockets **36**, 442 (1999).

[4] C. Park, *Nonequilibrium Hypersonic Aerothermodynamics*, 1st ed. (Wiley, 1990).

[5] A. Bourdon and P. Vervisch, Physical Review E **54**, 1888 (1996).

[6] C. Park, *Effect of Lyman Radiation on Nonequilibrium Ionization of Atomic Hydrogen*, AIAA Paper 2004–2277 (2004).

[7] C. O. Johnston, B. Hollis, and K. Sutton, Journal of Spacecraft & Rockets **45**, 879 (2008).

[8] I. Sohn, Z. Li, and D. A. Levin, Journal of Thermophysics and Heat Transfer **26**, 393 (2012).

[9] P. A. Gnoffo, C. O. Johnston, and R. A. Thompson, Journal of Spacecraft & Rockets **47**, 481 (2010).

[10] C. Park, Journal of Spacecraft & Rockets **44**, 24 (2007).

[11] B. Lopez and M. Panesi, *Study on Non-Boltzmann Models for Atomic Nitrogen*, AIAA Paper 2016–4431 (2016).

[12] M. Panesi and A. Lani, The Physics of Fluids **25** (2013).

[13] C. O. Johnston, Journal of Thermophysics and Heat Transfer **28**, 795 (2014).

[14] C. O. Johnston and A. Mazaheri, *Impact of Non-Tangent-Slab Radiative Transport on Flowfield-Radiation Coupling*, AIAA Paper 2017–1371 (2017).

TABLE V. Chemical kinetics for neutral species.

#	Reaction	$A_{f,i}$	$n_{f,i}$	$D_{f,i}$	$T_{f,i}$	Third Body, M	Ref.
1	$N_2 + M \leftrightarrow 2N + M$	3.01e+22	-1.60	1.132e+5	T_a	N, C, O	Park [4]
		6.0e+3	2.6	1.132e+5	T_{ve}	e^-	Bourdon et al. [19]
		7.0e+21	-1.60	1.132e+5	T_a	others	Park [4]
2	$N_2 + O \leftrightarrow NO + N$	6.0e+13	0.1	3.80e+4	T_{tr}		Fujita et al. [20]
3	$NO + M \leftrightarrow N + O + M$	4.40+16	0.00	7.55e+4	T_a	N, C, O, NO, CO_2	Johnston and Brandis [21]
		2.0e+15	0.00	7.55e+4	T_a	others	Johnston and Brandis [21]
4	$O_2 + M \leftrightarrow 2O + M$	1.0e+22	-1.50	5.936e+04	T_a	N, C, O	Park [4]
		2.0e+21	-1.50	5.936e+04	T_a	others	Park [4]
5	$O_2 + N \leftrightarrow NO + O$	2.49e+9	1.18	4.01e+3	T_{tr}		Bose & Candler [22]

TABLE VI. Chemical kinetics for ionized species.

#	Reaction	$A_{f,i}$	$n_{f,i}$	$D_{f,i}$	$T_{f,i}$	Ref.
6	$N + N \leftrightarrow N_2^+ + e^-$	4.40e+07	1.5	6.75e+4	T_{tr}	Park et al. [23]
7	$N + O \leftrightarrow NO^+ + e^-$	5.30e+12	0.0	3.19e+4	T_{tr}	Park et al. [23]
8	$N + e^- \leftrightarrow N^+ + 2e^-$	2.5e+34	-3.82	1.682e+5	T_{ve}	Park [4]
9	$N^+ + N_2 \leftrightarrow N_2^+ + N$	1.00e+12	0.5	1.22e+4	T_{tr}	Park [4]
10	$N_2 + O^+ \leftrightarrow N_2^+ + O$	9.10e+11	0.36	2.28e+4	T_{tr}	Park [4]
11	$NO + O^+ \leftrightarrow N^+ + O_2$	1.40e+5	1.9	2.66e+4	T_{tr}	Park [4]
12	$NO^+ + N \leftrightarrow N_2^+ + O$	7.20e+13	0.0	3.55e+4	T_{tr}	Park [4]
13	$NO^+ + N \leftrightarrow O^+ + N_2$	3.40e+13	-1.08	1.28e+4	T_{tr}	Park [4]
14	$NO^+ + O \leftrightarrow N^+ + O_2$	1.00e+12	0.5	7.72e+4	T_{tr}	Park [4]
15	$NO^+ + O \leftrightarrow O_2^+ + N$	7.20e+12	0.29	4.86e+4	T_{tr}	Park [4]
16	$NO^+ + O_2 \leftrightarrow NO + O_2^+$	2.40e+13	0.41	3.26e+4	T_{tr}	Park [4]
17	$O + O \leftrightarrow O_2^+ + e^-$	7.10e+02	2.7	8.06e+4	T_{tr}	Park et al. [23]
18	$O + e^- \leftrightarrow O^+ + 2e^-$	3.9e+33	-3.78	1.585e+5	T_{ve}	Park [4]
19	$O_2^+ + N \leftrightarrow O_2 + N^+$	8.70e+13	0.14	2.86e+4	T_{tr}	Park [4]
20	$O_2^+ + N_2 \leftrightarrow N_2^+ + O_2$	9.90e+12	0.0	4.07e+4	T_{tr}	Park [4]
21	$O_2^+ + O \leftrightarrow O^+ + O_2$	4.00e+12	-0.09	1.80e+4	T_{tr}	Park [4]
22	$O_2 + e^- \leftrightarrow O_2^+ + 2e^-$	2.19e+10	1.16	1.30e+5	T_{ve}	Teulet et al. [24]

[15] E. Whiting, C. Park, Y. Liu, J. Arnold, and J. Paterson, *NEQAIR96, Nonequilibrium Radiative Transport and Spectra Program: User's Manual*, NASA RP 1389 (1996).

[16] A. Mazaheri, P. A. Gnoffo, C. O. Johnston, and B. Kleb, *LAURA Users Manual*, NASA TM 2013-217800 (2013).

[17] P. A. Gnoffo, R. N. Gupta, and J. L. Shinn, *Conservation Equations and Physical Models for Hypersonic Air Flows in Thermal and Chemical Nonequilibrium*, NASA TP 2867 (1989).

[18] T. K. West, C. O. Johnston, and S. Hosder, Journal of Thermophysics and Heat Transfer **31**, 294 (2017).

[19] A. Bourdon and P. Vervisch, Physics of Plasmas **4**, 4144 (1997).

[20] K. Fujita, T. Yamada, and N. Ishii, *Impacts of Ablation Gas Kinetics on Hyperbolic Entry Radiative Heating*, AIAA Paper 2006–1185 (2006).

[21] C. O. Johnston and A. M. Brandis, Journal of Quantitative Spectroscopy and Radiative Transfer **149**, 303 (2014).

[22] D. Bose and G. V. Candler, Journal of Chemical Physics **16**, 6136 (1997).

[23] C. Park, Journal of Thermophysics and Heat Transfer **7**, 385 (1993).

[24] P. Teulet, J. J. Gonzalez, A. Mercado-Cabrera, Y. Cressault, and A. Gleizes, Journal of Physics D: Applied Physics **42**, 1 (2009).